

## Journal Pre-proof

Experimental study of an implantable fiber-optic microphone on human cadavers

Zoran Djinović , Robert Pavelka , Miloš Tomić , Georg Sprinzl ,  
Julia Gertrud Müller , Hannes Traxler

PII: S0378-5955(21)00185-4  
DOI: <https://doi.org/10.1016/j.heares.2021.108351>  
Reference: HEARES 108351



To appear in: *Hearing Research*

Received date: 6 August 2020  
Revised date: 17 August 2021  
Accepted date: 1 September 2021

Please cite this article as: Zoran Djinović , Robert Pavelka , Miloš Tomić , Georg Sprinzl ,  
Julia Gertrud Müller , Hannes Traxler , Experimental study of an implantable fiber-optic microphone  
on human cadavers, *Hearing Research* (2021), doi: <https://doi.org/10.1016/j.heares.2021.108351>

This is a PDF file of an article that has undergone enhancements after acceptance, such as the addition of a cover page and metadata, and formatting for readability, but it is not yet the definitive version of record. This version will undergo additional copyediting, typesetting and review before it is published in its final form, but we are providing this version to give early visibility of the article. Please note that, during the production process, errors may be discovered which could affect the content, and all legal disclaimers that apply to the journal pertain.

© 2021 Published by Elsevier B.V.

1 Experimental study of an implantable fiber-optic microphone  
2 on human cadavers

3 Zoran Djinić<sup>a</sup>, zoran.djinovic@acmit.at, Robert Pavelka<sup>b</sup>, Miloš Tomić<sup>c</sup>, Georg Sprinzl<sup>d</sup>, Julia  
4 Gertrud Müller<sup>e</sup>, Hannes Traxler<sup>e</sup>

5 <sup>a</sup>ACMIT GmbH, Viktor Kaplan Str. 2, 2700 Wiener Neustadt, Austria

6 <sup>b</sup>ENT specialist, Grünbeckgasse 15, 2700 Wiener Neustadt, Austria

7 <sup>c</sup>Institute of Technical Sciences of SASA, Kneza Mihaila 35, 11000 Belgrade, Serbia

8 <sup>d</sup>University Hospital St. Pölten, Dunantplatz 1, 3100 St. Pölten, Austria

9 <sup>e</sup>Medical University of Vienna, Department of Anatomy, Centre for Anatomy and Cell Biology, Waehringerstrasse 13, 1090  
10 Vienna, Austria

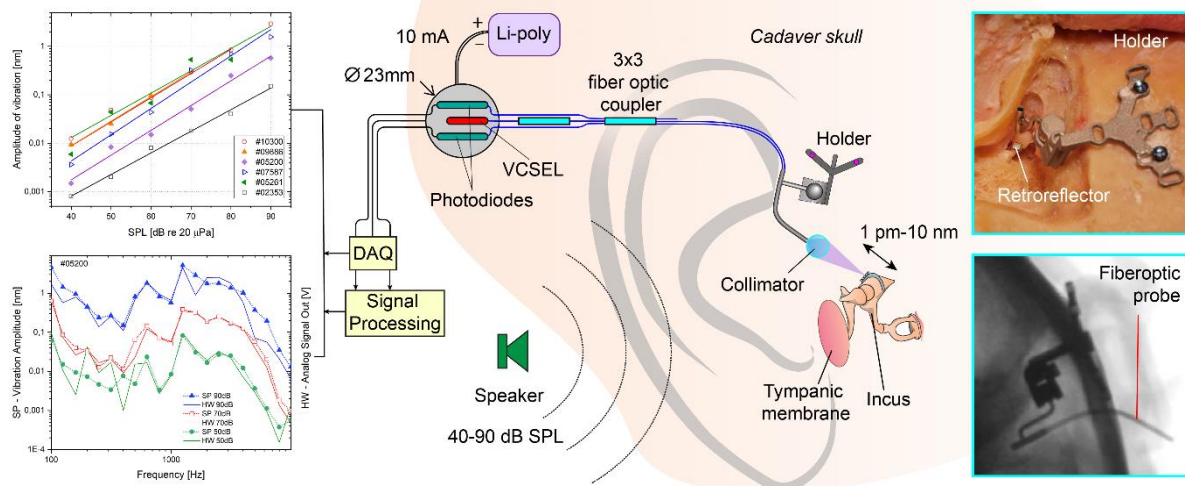
11  
12 Corresponding author.

## 13 Highlights

- 14 • Fiber-optic microphone meets most of demands for totally implantable hearing  
15 aids
- 16 • Dramatically reduced overall size of the microphone case allows easy implantation
- 17 • Flexible construction of the microphone makes a quick and reliable implantation
- 18 • High sensitivity and dynamic range of the microphone assure high sound fidelity

## 22 Graphical abstract

23 We present the results of experimental study a novel optical vibrometer aimed to be used as a  
24 totally implantable fiber-optic microphone for hearing aids. The sensor posted inside the  
25 human cadaver middle ear, detects the amplitude of the incus vibrations, produced by an  
26 external acoustical source.



1

2

3

4

5

## 6 Abstract

7 In this paper, we present the results of an experimental study about a novel fiber optical vibrometer, aimed to  
 8 be used as a totally implantable fiber-optic microphone for hearing aids. The sensor head, implanted inside the  
 9 human cadaver middle ear, detects the amplitude of the incus vibrations, which are produced by an external  
 10 acoustical source. The probe beam of coherent vertical cavity surface emitting laser (VCSEL) radiation is  
 11 directed to the incus and the phase-modulated reflected beam is captured and demodulated. The problem of  
 12 interferometric fading was solved using two quasi-quadrature signals, passively produced by the 3x3 single-  
 13 mode fiber-optic coupler, processed by a special embedded algorithm. The implanted optoelectronic module

works with very low-power consumption, performs real-time signal processing and outputs an analogue signal proportional to the incus vibration. The amplitude of the incus vibrations at different sound pressure levels (SPL) from 40 to 90 dB and at frequencies from 100 Hz to 10 kHz were measured by the implanted system. The system was evaluated on five cadaver skulls. The measured amplitudes were in the range of 1 pm to 5 nm, depending on the subjected skull and the applied sound pressure.

## Keywords

Implantable microphone; Fiber-optic sensors; Interferometry; Hearing aids; Cochlear implant.

## 1. Introduction

Many people all around the world are affected by hearing insufficiency caused by either middle ear diseases, malformation, or sensorineural impairment. The modern lifestyle and everyday urban noise pollution, especially in some cities of the developed countries, appear as an environmental hazard, which accelerates the hearing losses of their citizens (Hammer et al, 2014). It is estimated that more than 10 % of the global population is affected by partial or total hearing losses (Young et al., 2019; Park et al., 2018; Gesing et al., 2018). Most of them are old people over the age of 65 years (Haynes et al., 2009; Park et al., 2007). However, hearing loss affects children as well including neonates, which obstructs the normal speech development and communication (Faes et al., 2019). A big communication disorder can also be induced by sudden deafness associated with a rapid hearing loss (Zhang et al., 2019). All of these may further induce a number of social problems including poor education, stigmatization, difficult incorporation into society, and eventually marginalization of such children and adults (Lieu, 2004).

A common way to perform a hearing rehabilitation for people with moderate hearing loss is by conventional hearing aids (CHAs), which are externally worn, either behind-the-ear or in-the-canal types. However, they are associated with many drawbacks, including occlusion of the external auditory canal, chronic otitis, insufficient high-frequency gain, feedback, unnatural sound quality and bad speech comprehension, improper localization of sound, etc. Some people are not able to wear it, because of the too narrow ear canal, or intolerance to the device material. In addition, discomfort, social stigma and constraints caused by failure to resist water in daily activities such as working in a humid environment, bathing, showering and swimming, by handling and maintaining of the device, failure by occlusion of ear wax, are the main reasons for rather frequent rejection of this kind of hearing aids (Silverstein et al., 2005; Bittencourt et al., 2014; Zwartenkot, 2017).

Many of these drawbacks are resolved by partially implantable hearing aids in which the microphone, audio processor and battery are placed externally in the temporal or parietal region of the head, while the transducer is placed internally. The sound signal is transduced transcutaneous to the transducer via an induction coil. Active middle ear implants (AMEI) (Shohet et al., 2018) for mild to moderate conductive hearing loss amplify the acoustic vibrations of the cochlea fluid acting on an ossicle (Ototronix Maxum, Saint Paul, USA; Cochlear MET and Codacs™, Cochlear Ltd., Sydney, Australia; Rion Device E-type, RION Co., Ltd., Tokyo, Japan; Vibrant Soundbridge™, Med-El, Innsbruck, Austria) (Grossöhmichen et al., 2015; Klein et al., 2012; Komori et al., 2010), the round window membrane (Vibrant Soundbridge, Med-El, Innsbruck, Austria) (Bruchhage et al., 2017; Klein et al., 2013) or the temporal bone in the bone conduction implants (BCIs) (active: Baha Connect, Cochlear Ltd., Sydney, Australia; Oticon Ponto and Oticon PCI Best Transducer, Smorum, Denmark; Bonebridge, Med-El, Innsbruck, Austria and passive: Baha Attract, Cochlear Ltd., Sydney, Australia and Sophono Alpha, Colorado, USA) (Tisch, 2017; Zernotti et al., 2015). In turn, the cochlear implants (CIs) stimulate the hearing nerves electrically by electrodes in case of severe to profound sensorineural hearing loss and deafness (Seong et al., 2019; Calero et al., 2018). The cochlear implants are accepted worldwide for the clinical treatment not only of adults, but also of children with inborn or acquired profound sensorineural hearing loss or deafness even in the first years of childhoods (Dettman et al., 2016), which allows a normal speech development and success in school education.

To overcome the drawbacks associated with conventional or partially implantable hearing aids, a totally implantable hearing aid (TIHA) would be an ideal solution. The following advantages of the TIHA appear as the most important. Natural sound and missing occlusion effect and distortions from head touching and vulnerability to damage due to external impacts (Woo et al., 2015) lead to a better sound quality and hearing perception. Noise due to wind will be greatly reduced. The quality of life of the patient will be significantly improved using a TIHA since there are no more external parts of the device. The user can sleep without inconvenience, can wear helmet, perform normal daily activities, including those related to continuous use in a humid and watery environment. Also, since there are no more cosmetic issues and stigmatization, the patient's self-confidence and social inclusion will be increased.

Totally implantable hearing aids (TIHAs) were invented and implanted in small series of patients by different groups (Eggermont, 2017; Woo et al., 2015; Bittencourt et al., 2014; Kozłowski et al., 2014; Pulcherio et al., 2014; Haynes et al., 2009), but could not reach a large-scale production or spread. The most critical issues were the microphone and feedback problems in active middle ear implants. The implantable microphones have been

developed utilizing different approaches, advanced materials and technologies including piezoelectric ceramics, e.g., plumbum zirconate titanate (PZT) and micro-electro-mechanical systems (MEMS) among others (Gao et al., 2013; Gerard et al., 2017; Woo et al., 2013; Zargarpour et al., 2015; Woo et al., 2015; Jia et al., 2016). Despite that, nowadays there are just a few commercially available TIHA devices (Tisch, 2017; Pulcherio et al., 2014).

Depending on the implantation location there are two main groups of implantable sensors acting as microphones: subcutaneous and middle ear implanted sensors. The subcutaneous microphones have been designed as a common electric condenser microphone (ECM) working on the capacitive principle. The first subcutaneous implantable microphone, so called TICA (Totally Implantable Communication Assistance), was commercialized by Implex (Munich, Germany) in 2001 (Zenner et al., 2001). A hermetically packed titanium (Ti) cylinder capped with a 4,5 mm diameter Ti membrane was implanted in 20 patients under the skin of the ear canal, preserving the natural amplification of acoustical signals. Although an initial sensitivity of 5 dB ref. 1mV/Pa and a frequency range between 100 Hz and 10 kHz were reached with rather low power consumption smaller than 0,5 mW the product was withdrawn from the market. It experienced several drawbacks associated with deterioration of the original sensitivity induced by a scar tissue layer over the membrane, the signal distortion due to sound reflection from the tympanic membrane (TM) and feedback and body noise interference such as breathing, swallowing or the own voice, etc. Cochlear (Sydney, Australia) developed a capacitive microphone aimed to an invisible cochlear implant (CI), so called TIKI (Briggs et al., 2008), composed of an external and subcutaneous microphone implanted in just three patients under the skin at the temporal bone. Similar effect of sensitivity roll-off over the high frequency range was noticed. The next generation of the Cochlear's implantable device, so called Carina (Pulcherio et al., 2014), was also composed of two ECMs arranged to capture the external sounds and body signal simultaneously, which is then cancelled out from the output signal. In addition, the device was equipped with the signal processor, battery and transducer connected to one of the ossicles. Carina received the FDA approval in the USA and CE Mark in EU in 2007 (Bruschini et al., 2016).

The middle ear (ME) implantable sensors comprise of multiple designs and operation principles. Among them are electromagnetic (Maniglia et al., 2001) and optical sensors (Vujanic et al., 2002), which are tested in laboratory conditions utilizing the human temporal bones. The main drawback of the former, based on the permanent magnet of neodymium-iron-boron (NdFeB), was a limited frequency response between 250 Hz and 3 kHz and rather large power consumption of about 1 mW, while the latter demonstrated a broad frequency range

1 from 500 Hz to 10 kHz, but relatively low sensitivity and a large power consumption of 6,4 mW mostly induced  
 2 by laser current of 80 mA.

3 Micro-Electro-Mechanical-Sensor (MEMS) technology opened a new avenue in the field of the ME  
 4 implantable sensors aimed to TIHAs. The first prototype of an implantable sensor based on this technology was  
 5 the piezoresistive MEMS accelerometer, which was tested in the laboratory set-up using cadaveric TBs (Park et  
 6 al., 2007). Frequency response over 900 Hz to 7 kHz was obtained, although power consumption was higher  
 7 than 1 mW. A group of capacitive displacement sensors was developed utilizing the MEMS technology.  
 8 Basically, most of them were composed of a silicone substrate and diaphragm creating of two electrodes of a  
 9 condenser, which capacitance changes in dependence on the ossicle vibrations (Ko et al., 2009). Overall size of a  
 10 silicon chip was 2x2 mm and mass of about 25 mg. The silicon chip was coupled to an ossicle, e.g., umbo of the  
 11 human TB. Woo et al., 2013 proposed a capacitive microphone capable to measure the acoustic pressure in the  
 12 ME cavity over the wide frequency range from 100 Hz to 7 kHz and sensitivity of  $28 \pm 3$  dB, while power  
 13 consumption was slightly larger than 1 mW.

14 A group of piezoelectric force transducers have also been proposed for implantable ME sensors. A very  
 15 interesting solution of such an implantable microphone is applied in the Esteem® middle ear implant from  
 16 Envoy Medical Corp., White Bear Lake, USA (Pulcherio et al., 2014; Memari et al., 2011; Murali et al., 2009). It  
 17 is the first implant using the acoustic vibrations of the head of the incus for the microphone to be picked up by a  
 18 piezoelectric sensor in direct contact with the incus (Chen et al., 2004; Kozłowski et al., 2014). This avoids many  
 19 of the aforementioned drawbacks of subcutaneous microphones and takes advantage of the natural acoustic gain  
 20 of the outer ear and the eardrum especially in the high frequencies, but other problems arise in this system.  
 21 Besides the necessity of interruption of the ossicular chain to avoid feedback noise, the direct contact of the  
 22 piezoelectric sensor to the incus could become a problem possibly causing changes of the middle-ear impedance  
 23 on the vibrations, in a long-term loss of contact and function due to osteolysis of the bone. Contact pressure to  
 24 the bone can significantly rise due to comparatively large movements of the incus in some special circumstances  
 25 caused by atmospheric pressure changes like blowing the nose, aircraft flying, or using an elevator or a cable car  
 26 (Ihrle et al., 2016; Dirckx et al., 2006; Didyk, 2006; Tay et al., 1996; Hüttenbrink et al., 1988). Such large quasi-  
 27 static movements of the ossicles may eventually hinder the microphone operation.

28 Although technically suitable for implantation with sufficient acoustical sensitivity, the main drawback for  
 29 the majority of TIHA is the location of an implantable microphone subcutaneously on the head (Carina© MEI by

1 Cochlear Ltd., Sydney, Australia) (Haynes et al., 2009; Bruschini et al., 2009; Knoch et al., 2014; Pulcherio et  
 2 al., 2014), or in the outer ear canal (TICA by Implex, Munich, Germany) (Zenner et al., 2001; Leysieffer et al.,  
 3 2003). The soft tissue covering the microphone leads to a damping effect especially for high frequencies (Woo et  
 4 al., 2015; Seong et al., 2019). Another problem is the lack of directional properties and the acoustic disturbing  
 5 noise of the wind, body noise, headgear like a helmet or any touch of the head. Therefore, the Carina© MEI  
 6 implant has an additional external button audio processor for more challenging hearing situations. In the direct  
 7 comparison, the patients state that hearing is better with the external microphone in the button audio processor  
 8 than with the implanted microphone (Jenkins et al., 2008; Jenkins et al., 2007).

9 For cochlear implants, currently there is no fully implantable system available (Lenarz, 2017; Gerard et al.,  
 10 2017), due to some still existing technical issues. The main one is associated with an implantable microphone,  
 11 which is still unable to provide the initial set of parameters over a long-time operation inside the human body.  
 12 From the clinical point of view, an implantable microphone must demonstrate a high degree of biocompatibility,  
 13 absolute hermeticity, corrosion resistance against the body fluids, a sufficiently reduced overall size, which allow  
 14 easy implantation in the region of the middle ear (Calero et al., 2016). Recently, Gesing et al., 2018, summarized  
 15 the most critical technical requirements for an implantable microphone out of comprehensive literature data,  
 16 which concern the required bandwidth from 250 Hz to 8 kHz and dynamic range from 40 dB to 100 dB SPL re  
 17 20  $\mu$ Pa, overall dimensions of just a few millimeters in total and reduced power consumption to the range of  
 18 mW.

19 To solve most of the aforementioned problems our research team has been working for long time (Pavelka et  
 20 al., 2003; Tomic et al., 2017; Djinoić et al., 2018) on the development of an implantable contactless fiber-optic  
 21 sound sensing system based on the measuring of the acoustic vibrations of an ossicle in the middle ear. We  
 22 started with experiments in sheep, *in vivo* and post-mortem, to develop the technical system and to study the role  
 23 of tissue overgrowth, after implantation of the sensing fiber into the middle ear, on the signal quality in  
 24 correlation to the histological findings 2 to 5 months after implantation (Djinoić et al., 2018). The main  
 25 conclusion was that despite the tissue overgrowth over the fiber and the retroreflector clipped to the incus, we  
 26 still measured acoustic signals in these animals. Empowered by these results we continued our research on  
 27 human skulls in 2015.

28 The main advantage of our Totally Implantable Fiber Optic Sensor (TIFOS) is a contactless measuring of the  
 29 acoustic vibrations of an ossicle that prevents signal attenuation, due to damping effect caused by interaction



with the bone ossicles, skin and/or scar tissue. Furthermore, such an approach provides enough freedom for quasi-static movements of the ossicles being exposed to atmospheric pressure changes, or due to the growth of the skull in children. TIFOS leaves the whole hearing chain *intact*, which ensures the natural acoustic gain of the outer ear and the ear canal resulting in a better reproduction of high frequencies over the range of 1 to 6 kHz. This is of utmost importance for the good and natural speech and music perception of the TIFOS microphone that was experimentally proved by acoustic recordings presented in the supplement.

In this paper, we present the results of a preclinical study of our fiber-optic sound sensing system acting as an implantable microphone, which is designed to overcome most of the aforementioned drawbacks of existing microphones by its novel technical solution. A measurement setup has been established in the dissection room at the Centre for Anatomy and Cell Biology of the Medical University of Vienna for the audio testing in human cadaver skulls with a calibrated audiometer generating the pure tone stimuli from 40 to 90dB SPL over the frequency range of 100 Hz to 10 kHz. Many audio recordings playing versatile music sequences and speeches from near high-fidelity loudspeakers have been acquired. A round optoelectronic module packed in a biocompatible housing was tested and proved to perform on-line signal processing of raw interference data and to deliver output microphone signals. The amplitude of the incus vibrations was calculated, and the frequency response and audio recordings were determined. The natural ear canal resonance (REUR = real ear unaided response) frequency response was correlated to the frequency response. Equidistant frequency response curves, which were acquired at different SPLs, confirmed good linearity of the sensing system. The measured amplitudes were found to be in the range between 1 pm and 1 nm, under the sound excitation of 40-90 dB SPL @ 1kHz, respectively. The whole device drew less than 10 mA from an implantable Li-ion battery cell.

## 2. Materials and methods

### 2.1 Principle of operation and configuration of the sensing system

Fig. 1 schematically presents the sensing configuration, which has the structure of a Michelson interferometer based on a single-mode 3x3 fiber-optic coupler (FOC 3x3). The middle input arm of the FOC 3x3 is connected to a pigtailed vertical cavity surface-emitting laser diode (VCSEL), acting as a coherent light source. An optical isolator (OI) is interposed to protect VCSEL against back-reflected radiation. The two output arms of FOC 3x3 are the sensing (SA) and reference arm (RA) of the Michelson interferometer. The third output arm is inactive in this configuration. It is cleaved at 8°, to suppress back reflections, parasitic interferences, and noise generation.

Fig.1

A spherical collimator (C) at the end of the sensing arm (SA) directs about one-third of the total optical power to a vibrating target (T) and recollects a small part of the reflected radiation. Another third of the total optical power, which is in the reference arm (RA), returns to the coupler after reflection from the golden mirror (M), sputtered at the end of the RA. The length of the RA is approximately the same as the length of the SA, so the optical path difference (OPD) in the interferometer is smaller than the coherence length of the VCSEL. Looking back at the coupler input side, we see that two other “input” arms carry coherent mixtures of the SA and the RA optical radiation to the photodiodes PD1 and PD2. The vibration of the target changes the OPD and two quasi-quadrature signals (X and Y) are detected by photodiodes (Koo et al., 1982):

$$X(t) = V_{DC1} + V_{A1} \cos\left(\frac{4\pi}{\lambda} \cdot A \sin \omega t + L(t)\right) \quad (1)$$

$$Y(t) = V_{DC2} + V_{A2} \cos\left(\frac{4\pi}{\lambda} \cdot A \sin \omega t + L(t) + \psi\right)$$

where  $A$  and  $\omega$  are the amplitude and the frequency of the target vibration;  $\lambda$  is the VCSEL wavelength;  $\psi$  is the static phase shift produced by the FOC 3x3 coupler;  $V_{DC1}$  and  $V_{DC2}$  are non-interferometric DC levels;  $V_{A1}$  and  $V_{A2}$  are interferometric amplitudes, which depend on the target reflection, the coherence degree and the state of polarization alignment between the SA and RA waves;  $L(t)$  represents a random motion of the target, caused by external influences. The maximum slope of the curve defined by Equation (1) determines the maximum sensitivity of the interferometric system in the case of measuring small vibrations. The maximal sensitivity  $S$  is the first derivative of the photodiode signal  $X$  (or  $Y$ ) with respect to the amplitude of vibrations  $A$ :  $S = \partial X / \partial A = 4\pi V_{A1} / \lambda$ , in the specific working points where the condition  $\{L(t) + \psi = (2k+1) \cdot \pi/2, k=0,1,2,\dots\}$  is satisfied. The random term  $L(t)$  causes wobbling of the working point, so the sensitivity  $S$  is always changing and the amplitude  $A$  cannot be extracted using either the  $X$  or  $Y$  signal alone.

The reconstruction of the full target motion can be obtained by a suitable processing algorithm applied to the  $X$  and  $Y$  signals (Tomic et al., 2017). In this process, the dependence on the variables  $V_{A1}$ ,  $V_{A2}$ ,  $V_{DC1}$ , and  $V_{DC2}$  will be removed and an output signal, proportional to the interferometer OPD (the term with  $A$ ,  $\omega$ ,  $L(t)$  in Eq. (1)), will be obtained. The main steps in the signal processing are illustrated in Fig. 1, by four white boxes.

When the signals X and Y are connected to the vertical and the horizontal input of an oscilloscope, they form a specific Lissajous figure on the screen – an ellipse inclined at an angle of  $120^\circ$ , as shown in the upper-left part of Fig. 1. As the target moves back and forth towards the laser beam, a bright oscilloscope dot draws an ellipse. Slow displacement with a large amplitude makes one or more ellipses, while small vibrations, characteristic for the middle ear bones, cause a quivering of the dot along the circumference of the ellipse, in the tangential direction. The size of the ellipse depends on  $V_{A1,2}$ , the amplitude noise in the signals X and Y determines the thickness of the ellipse. It is easy to estimate a coarse signal-to-noise ratio (SNR) by observing the relationship between the diameter and the thickness of the ellipse on the oscilloscope screen. In the process of aiming the laser beam at the target, the surgeon is trying to achieve the largest and the thinnest ellipse, maximizing in that way the SNR. It is interesting to note that the amplitude noise of the laser, since it causes only the radial motion of a point on the ellipse, does not have a significant influence on the noise in the demodulated phase signal.

The next steps in the signal processing include the removal of DC levels ( $V_{DC1}$  and  $V_{DC2}$ ), equalization of the interferometric amplitudes ( $V_{A1}$  and  $V_{A2}$ ) and converting the coupler-dependent phase angle ( $\Psi$ ) between two signals to the angle of  $\pi/2$ . As a result, we obtain pure quadrature signals (I and Q), presented in Fig. 1 as a circle on the oscilloscope screen. I and Q are intermediate results, which were used in the earlier stage of the system development as a control of the success of the applied algorithm. The final step in signal processing is the application of the arc-tangent function (ATAN) to obtain the phase angle (PHI), starting from the quadrature signals I and Q. The PHI output signal contains the vibration of the incus  $A \cdot \sin \omega t$ , which is caused by acoustic excitation and the movement of greater amplitude  $L(t)$ , induced by changes in air pressure, stresses while swallowing, infrasound vibration, etc., which can now be separated by simple acoustic bandpass filtering.

The sensing system, schematically presented in Fig. 2., consists of four main modules: 1) the optoelectronic and signal processing module, packed in a round case, denoted as TIFOS, 2) the fiber-optic module composed of an optical isolator, a 3x3 fiber-optic coupler, optical fibers, insertion tube and collimator, 3) the optomechanical holder & reflector and 4) the power supply module.

Fig. 2

The optoelectronic and signal processing module of the TIFOS system, presented in Fig. 3a, is a round shape PCB, 23 mm in diameter, packed in a round case with 26 mm in diameter and 6.5 mm in height. The case is made

of polycaprolactone (PCL), which is a biocompatible material, see Fig. 4c. Some other materials and manufacturing technologies were tested, including 3D printing and machining of titanium and maraging stainless steel (1.2709). Although titanium is already proved as a biocompatible material, PCL was chosen for the TIFOS case to avoid artifacts in CT or MRI diagnosis of head and brain. Maraging stainless steel was chosen as the main material for the optomechanical holder due to cheaper production, although titanium could be used in the future.

The optical source is a single-mode pigtailed VCSEL diode (RC220471-OLmini, RayCan Co Ltd., Daejeon, Korea), emitting at 1310 nm. The pigtail optical fiber was connected to the input arm of a 3x3 single-mode fiber optic coupler (3x3) via an optical isolator (OI) (both from Optosun Technology Limited, Shenzhen, China). The receivers of optical signals are two pigtailed InGaAs photodiodes (Optosun Technology Limited). All of the optical fibers are the same type – single-mode SMF-e28 (Corning Inc., New York, NY, USA), with core/cladding/coating diameters of 10/125/250  $\mu\text{m}$ , respectively.

The VCSEL was driven by a home-made low-noise driver, designed using the low-noise and low-power operational amplifier LT6013 (Linear Technology, Milpitas, CA, USA). The constant laser current was set to 3 mA, producing optical power of 240  $\mu\text{W}$  coming out of the fiber pigtail. Two photodiodes were connected to very low-power transimpedance amplifiers (TIA), designed with OPA333 (Texas Instruments, Dallas, TX, USA), giving the maximal voltage output of about 3V.

On-line signal processing: The TIA output signals,  $V_x$  and  $V_y$ , were digitized by a pair of low-power 16-bit analog-to-digital converter (ADC) (ADS8866, from Texas Instruments). The data streaming from ADC was fed to an ultra-low-power ARM microcontroller (MSP432P401, from Texas Instruments), where the before described signal processing was applied. The signal was sequentially processed in the real-time (“on-line”), at the level of one sample. The phase value, obtained at the end of the calculation, was sent to a low-power, 16-bit digital-to-analog converter (DAC) (DAC8411, Texas Instruments), where the analog voltage, which corresponds to the target movement, was generated. All signal processing operations on one ADC sample were finished before the next sample has been received from the ADC.

The algorithm embedded in the microcontroller takes about 1000 clock cycles to process the signals. The most computationally demanding part of the processing is the ATAN calculation. To reduce this processing time, the four-quadrant, second-order approximation of ATAN from (Lyons, 2012) was used. This approximation includes, apart from addition and subtraction operations, only one division of numbers, introducing a negligible error, which cannot be noticed in the final acoustical signal. The master clock of the microprocessor was chosen as a trade-off

between the sampling frequency and the whole device power consumption. The master clock was set to 32 MHz, to keep the total current of device below 10 mA (note that the microprocessor power consumption linearly increases with the clock frequency). That value of the clock allows the highest sample rate of 32 kS/s, which, according to Nyquist's criterion, is sufficient for proper digitalization of the input signal bandwidth of 16 kHz. However, the nature of the interferometric signal regularly implies at least one frequency doubling, even for small signals – so the useful phase signal bandwidth was in effect 8 kHz.

The analog signal from DAC was finally filtered by the hardware band-pass filter, to suppress noise and remove the incus slow drift. This filter was realized by two low-power operational amplifiers (OPA2333, Texas Instruments), with low and high cut-off frequency at 100 Hz and 8 kHz, respectively. All signal processing operations were completed within an ADC sampling interval (31.25  $\mu$ s) and the overall delay from the incus vibration to the analog output signal from the DAC was below 100  $\mu$ s (ADC + signal processing + DAC).

Off-line signal processing: Besides being routed to the ADC, the TIA output signals ( $V_x$  and  $V_y$ ) are also wired out of the TIFOS casing (green and yellow wires in Fig 3a.) and acquired by an external 16-bit digitization card (DAQ, from National Instrument, Austin, TX, USA). The output analog phase signal, from DAC ( $V_\phi$ ), was also digitized by DAQ. The sampling rate was set to be the same as in the embedded ADC – 32 kS/s. These signals were recorded and used later for the off-line signal processing, according to the same algorithm as in the microcontroller. The off-line processing was performed using the MATLAB software package (MathWorks Inc., Natick, MA, USA). The main difference between two processing was that in the off-line processing no approximation was used for the ATAN function. The purpose of this double processing was to check the correctness of the embedded algorithm operation, by comparing the real-time output signal  $V_\phi$  with the result of the phase angle calculated in MATLAB.

The raw photodiode signal outputs were also used during the aiming and fine adjustment of the sensing fiber (i.e., the emitted optical beam) versus the retroreflector, by visual tracking of the quasi-quadrature signals (PD1 and PD2, see Fig. 1) in real-time, using an oscilloscope. When the optical beam hits the retroreflector close to the optimal angle and spot, the raw photodiode signals go higher. The size of the ellipse on the oscilloscope X-Y mode screen is maximal and can reach 3V at the optimal adjustment. Once the fine tuning was finished, the optimal position of the fiber was locked by a screw on the optomechanical holder.

The power consumption of the TIFOS system, including signal processing, was about 10 mA. Since the system is supplied by the nominal battery voltage of 3,6 VDC that corresponds to the overall power consumption of about

36 mW. The VCSEL takes about 11 mW and the rest is mostly related to the microprocessor and the on-line signal processing. Some reductions of the overall power consumption are envisaged in the future work. The VCSEL drive current can be reduced to about 2 mA, to be just above the threshold (that is, according to the manufacturer's data for this type of VCSEL, between 1 mA and 2 mA). Also, the VCSEL can be driven in the pulsed mode, instead of current continuous operation. A power saving of about 50% is also expected from the new generation of the ultra-low-power microcontrollers. In that way, we expect that the total consumption of a future TIFOS system can be around 15-18 mW. This is still much higher than other systems met in the literature (Calero et al., 2018), but would enable autonomous operation of about 70-80 hours from the battery Quallion QL0370 (EnerSys, Reading, PA, USA), which is currently used in the TIFOS system.

-----

Fig. 3

The fiber-optic part is composed of the optical isolator, the 3x3 fiber-optic coupler (acting as splitter/combiner of the interferometer), the sensing fiber probe with a collimator and the reference fiber arm. The sensing and reference fiber arms were encapsulated into a medical-grade Polydimethylsiloxane (PDMS) (NuSil MED-6219, Avantor Inc., Radnor, PA, USA), about 100 mm in length and 1 mm in diameter, which was acceptable for the implantation. The end of the probe fiber arm was sealed into a graduated curved medical needle (insertion needle), 1 mm in diameter, Fig. 4a, and 4b. Figure 3b shows the sensing and reference arms before setting into the insertion needle. The needle has a pre-curved angle of about 60° relative to the axis (see Fig. 4b), to follow the skull anatomy, and can be easily adjusted by bending, according to the skull anatomy, if necessary.

Such a compact and robust design significantly decreases the overall noise in the system. The sensing fiber was terminated by a spherical collimator of 450  $\mu\text{m}$  in diameter, with the working distance of about 2.5 mm (Corning Inc.). Such a relatively long working distance make adjustment easier, because of very good spot visibility. The insertion needle was marked at every 0.5 mm, to help in adjusting the right distance between the fiber-optic probe and retroreflector under the microscope. It also makes the whole surgical procedure easier and faster. The reference fiber arm was terminated by a golden mirror of about 200 nm in thickness, made by sputtering on the fiber tip. The fiber tip is additionally protected by encapsulation into the aforementioned implantable grade PDMS. The same protecting method is used for encapsulating the glass beads of the retroreflector. In our *in-vivo* experiments performed on sheep (Djinovic et al., 2018), we were able to measure acoustical signals even 2 to 5 months after implantation on sheep, despite of the tissue growth found over the

collimator and retroreflector. So, we believe that the possible issues of tissue overgrowth as well as moisture interaction with the implanted optical and fiber-optic elements, will not be critical.

The optomechanical holder, as shown in the insets of Fig. 4, is implanted into the mastoid cavity after mastoidectomy and posterior epitympanotomy, and fixation of the retroreflector to the short process of the incus. The holder was made by 3D laser printing from maraging stainless steel. The base platform is firmly fixed to the temporal plane by titanium screws. A medical-grade stainless steel ball, 4 mm in diameter, acts as a pivot element, enabling fine adjustment of the fiber-optic probe. The ball is connected to the guiding needle, which accepts the insertion needle and directs the fiber-optic probe to the incus, via an S-shape rod of different lengths from 4 to 8 mm. The rod length depends on the anatomy and distance of the temporal plane to the incus. Fine adjustment of the fiber-optic probe versus retroreflector was performed by rotation of the ball and its fixation by a screw. In the adjustment procedure, a constant acoustical signal of 70 dB SPL was generated by the loudspeaker, at 1 kHz, and two photodiode electrical signals have been monitored on the oscilloscope screen in real time. Once the signals were as high as possible and the quadrature ellipse was clear (large and thin), the screw over the ball clamp was locked. The holder is very robust and provides a stable position after adjustment.

The retroreflector, shown in Fig. 4a, was a 1.4 x 1.4 mm<sup>2</sup> piece of 3M tape, covered by 50  $\mu$ m barium-titanite glass beads, which was adhesively bonded to a clip of stainless-steel strip of 100  $\mu$ m in thickness. The strip was manufactured by laser cutting. The form of the stainless-steel clip can be fine-tuned to follow the anatomy of the short process, ensuring a firm and long-term fixation to the incus. This retroreflector has been proved as the best one for providing a stable interference signal and proper operation of the microphone. The metalized bottom hemisphere of the glass beads behaves as a mirror ensuring the reflection of the light beam under the same angle as it has impinged to the retroreflector. So, the orientation of the plate does not have to be orthogonal to the laser beam, but can vary in a wide range of at least  $\pm 15^\circ$ . The experiments have shown that such a retroreflector can easily be mounted onto the incus, via the short process. The somewhat elastic material can be preformed on the table and clipped to the short process, then slipped towards the body of the incus. Because of the conical form of the short process, this increased the strength of fixation and kept the original position during the whole time of the investigation. The overall size of the retroreflective area is large enough to enable fast aiming of the laser beam.

The implantable rechargeable battery Quallion QL0370, with the nominal voltage of 3.6 VDC and capacity of 410 mAh, is a relatively large prismatic Li-ion cell with outside dimensions of 9.6x18x29.6 mm<sup>3</sup>. Since the

TIFOS device draws about 10 mA, this battery allows permanent operation over about 40 hours before recharging. Being rather bulky, this battery is not foreseen for the implantation in the skull. The battery could be implanted subcutaneously in the subclavicular region or elsewhere, as it is usual at present for the hypoglossal nerve stimulator (Wray et al., 2016). This location is clinically more convenient for battery loading and surgical replacement. The problem of torsion of the conductors by head and neck motions is already resolved by this mentioned hypoglossal nerve stimulators for the treatment of obstructive sleep apnoea from Inspire® Upper Airway Stimulation System (Inspire Medical Systems, Inc., Minneapolis, MN, USA), or aura6000™ (LivaNova PLC, London, UK) by using a spiral conductor to allow movements. This is inserted by a subcutaneous tunnel to the implantation site of the battery either in the subclavicular or in the lateral supraclavicular area accessed by a separate skin incision. In the future, we will reduce the total power consumption and use a smaller battery.

## 2.2 System calibration

The proper operation of the TIFOS system has been tested at first in our optical laboratory using a calibrated PZT actuator (Physik Instrumente (PI) GmbH & Co. KG, Karlsruhe, Germany) equipped with a retroreflective tape as a target. The actuator, previously calibrated by a Polytec Laser Doppler Vibrometer (LDV, Polytec GmbH, Waldbronn, Germany) was driven by the sinusoidal signal in the frequency range from 500 Hz to 10 kHz, producing in that way a target displacement of 0.3 to 10 nm. We used the PZT vibrating at 1 kHz, with the RMS amplitude of 7.4 nm, as a reference target for routine checking of the TIFOS system before every experiment on cadaver.

## 2.3 Surgical operation and implantation procedure

The experimental study of the TIFOS system has been performed in a dissection room at the Centre for Anatomy of the Medical University of Vienna, under relatively quiet environmental conditions, rarely interrupted by external noises. The system has been evaluated in 16 cadaver skulls. The final optimized TIFOS system was implanted in the last five cadavers only and we are presenting here only these data. Figure 4 represents a typical test arrangement in the dissection room.

-----

Fig. 4

The test procedure started with the surgical preparation of a cadaver skull. Most skulls were previously frozen unfixed skulls and defrosted several hours before the experiment, some were fresh cadavers within 1 or 2



days after death. The experiments did not show any significant differences in results between the frozen and the fresh cadavers. At first, the outer ear canal was cleaned, and the eardrum was inspected to be transparent and intact. Then, the surgeon (R.P.) performed a mastoidectomy and a posterior epitympanotomy, reaching as far anterior as possible to the zygomatic radix with an exposition of the short process and the body of the incus. The clip with the retroreflector was preformed on the table to the individual form of the short incus process and clipped to the short process, clamped, and slipped onto the body of the incus. Because of the conical form of the short process, it was fixed firmly. In principle, the retroreflector should approximately be orthogonal to the sensing fiber, but there is a wide degree of freedom of at least  $\pm 15^\circ$ , as has been explained before. The surgical procedure usually took about an hour and a half.

The short process of the incus was chosen to be the target due to the most suitable access to a part of the ossicular chain with a straight collimator. Also, this place allows a separation of a few millimeters between the end of the collimator and the ossicle, which is sufficient to avoid, or at least, minimize bridge-building of scar tissue between them during the patient's healing time, thus minimizing light scattering.

The optomechanical holder was then fixed into the bone of the temporal squama with titanium screws, in a place where the guiding tube was in a most anterior position, and the incus was visible through the hole of the guiding tube. Now, the holder was ready to accept the fiber-optic probe by introducing the straight part of the bent insertion needle into the guiding tube. The optimal distance between the collimator and retroreflector was about 2.5 mm, but distances between 1 to 4 mm did not make any significant difference in proper functioning. Therefore, it was sufficient to judge the distance optically by the microscope guided by the 0.5 mm marks onto the insertion needle. The fitting inside the guiding needle was so precise and strong, hence no additional fixation was necessary. However, it could be fixed by any means, e.g., screwing, clamping, welding, etc. The permanent functionality of the microphone is allowed by the large coherence length of the light source (VCSEL), extending over 5 mm, which is larger than the collimator working distance. The condition for the interference is therefore preserved over the largest distance between the collimator and retroreflector. The assembly turned out to be very reliable, assuring a long-term stable position and distance between the collimator and retroreflective target.

The distance between the sensing fiber probe and retroreflector should be relatively large for several reasons. First, safety - the distance should prevent any physical contact of the collimator and the retroreflector that can happen because of movement of the incus due to sudden alternation of environmental pressure. The variation of differential pressure on tympanic membrane can be several orders of magnitude larger than the acoustically

induced pressure levels. It is typically caused by ambient pressure changes, when blowing the nose or taking an elevator, flying, or even changing the body posture (Ihrle et al., 2016; Dirckx et al., 2006). Many authors have investigated the influence of the quasi-static pressure change on the mobility of the ossicles in the middle ear. Among them, Hüttenbrink et al., 1988 found a rather large umbo displacement of about -400  $\mu\text{m}$  and 200  $\mu\text{m}$  for negative and positive applied pressure of  $\pm 4$  kPa in the ear canal, respectively. Similarly, Tay et al., 1996 measured mobility of the malleus and incus with varying middle ear pressures. The incus displacement was less than 100  $\mu\text{m}$  for an applied pressure of -3 to +6 kPa. Second reason for setting a large distance is also essential – we want to diminish the danger of a bridge formation of scar tissue from the reflector to the collimator. That happens during the healing process *in vivo* (Djinović et al., 2018), causing scattering and damping the light intensity. Last but not least, this distance gives enough space for the growth of a child's head.

A model of the implantable grade silicone net, as a carrier of the encapsulated TIFOS optoelectronic module and the fiber-optic interferometer, with the sensing and the reference arms, enclosed into the medical grade stainless steel needle, is shown in Fig 4c. The TIFOS casing immersed in the silicon net is positioned behind the pinna. This should make easier the implantation process and the handling of the fibers.

## 2.4 Acoustic measurements

The integral frequency response of the TIFOS system and the outer & middle ear was measured and some speech and music recordings were taken under open mastoid cavity conditions. The measurement setup was based on the Affinity audiometer (Interacoustics A/S, Middelfart, Denmark) with REM440 Software, capable of performing testing using the generation of pure sinus tone stimuli of level from 40 to 90 dB SPL, in the frequency range of 100 Hz to 10 kHz, with an interval of 1/6 or 1/3 octave. The testing tone was generated by a JBL Control® CM52 loudspeaker (HARMAN International Industries, Inc., Northridge, CA, USA), positioned about 80 cm from the examined skull, Fig. 4. The output sound level was continuously monitored and automatically adjusted in real-time, using the reference microphone of the *in-situ* audiometry device headset (IHM60), positioned close to the entrance of the outer ear. We calibrated the sound generation system before each series of measurements. The frequency response was measured at 21 specific frequencies, for SPL ranging from 40 to 90 dB in steps of 10 dB, making 126 measurement points for each skull in total. The minimum specified SPL that Affinity audiometer was able to generate was 40 dB SPL. This value also was roughly the level of the environmental noise in the dissection room.

Music sequences, text readings, speeches, and interviews, which reflects a large range of frequency, loudness, and dynamics, have also been generated in the dissection room, by two high-quality stereo loudspeakers (GigaWorks T40 Series II, Creative Technology Ltd, Jurong East, Singapore) with frequency response 50 Hz – 20 kHz and 16 W RMS, to test the signal processing part of the sensing system. The average sound pressure level impinging the eardrum of the cadaver specimen was measured by a sound level meter (B&K Type 2250, Brüel & Kjær A/S, Nærum, Denmark), positioned beside the skull ear. The minimum and maximum dBA levels during the music playing were noted.

The NIDAQ 16-bit acquisition system and a PC for recording the two raw photodiode interference signals and the on-line processed analog audio signal can be seen on the right side in Fig.4. The signals have typically been acquired at 32 kS/Ch/s, in a time duration of about 30 s per recording. The raw photodiode signals were afterwards off-line processed in MATLAB, using the full arctan algorithm, and compared to the recorded analog output, to test the microcontroller firmware performance and quality of the abridged processing algorithm.

*The natural ear canal resonance, also named acoustic gain or REUR (Real Ear Unaided Response), was also measured. The REUR is different for every skull, due to the specific anatomy of the outer ear and ear canal. The REUR was measured by the tube microphone of the in-situ Affinity headset (IHM60) via a small silicon tube, whose tip was positioned in the ear canal close to the tympanic membrane. A constant sweep over the whole acoustic frequency range was made at 70 dB SPL. Beforehand, the tube microphone was calibrated to 70 dB SPL pantonal, then inserted. The correct sound intensity was checked and adjusted by the closed-loop in real-time, by the reference microphone of the Affinity system, posted close to the entrance of the outer ear canal, Fig. 4c.*

### 3. Results and discussion

Figure 5 summarizes the frequency responses of five cadaver skulls obtained at 80 dB SPL. There is also a response at 40 dB SPL, as an illustration of the bottom limit of measurement. The shapes of frequency response are similar for all subjected cadaver skulls. Most of them demonstrate a resonant frequency peak between 1000 Hz and 4000 Hz, reflecting the amplification effect of the ear canal. The sound pressure was generated by the sound generator Affinity audiometer over the frequency range from 100 Hz to 10 kHz. The real SPL arriving at the outer ear was monitored by a calibrated reference microphone built in the *in-situ* headset (IHM60) positioned close to the entrance of the outer ear canal (see Fig. 4c). In this way, using the closed-loop, the constant level of

SPL was maintained over all frequencies. Because of different points of measuring the REUR and frequency response, the compliance with frequency peaks in the acoustic measurements is not always very strict. The changes of natural resonance gain on the way between the eardrum and short process of the incus could not be measured and were never measured according to our knowledge and literature data. An example of this difference can be seen in skull #05200, which has a peak at about 1200 Hz., while the REUR peak appears at about 2000 and 4000 Hz (see Fig. S2). The resonant peak shift obtained in skull #05200 could be the result of small changes of the middle-ear impedance caused by the interaction of the bone ossicles and water traces left after the ear rinsing.

Figure 5 presents just five results of cadaver skulls at 80 dB SPL for the sake of illustration and clarity of the diagram. The other curves in 10 dB differences from 40-90 dB are strictly parallel to each other, as it is depicted in Fig. 6.

Fig. 5

There is a strong roll-off of the amplitude of vibrations in the high-frequency range. This response is determined by the mechanical response of the ossicle chain and by the electronic low pass analog filters of the TIFOS system, limiting maximal frequency to 8 kHz. The response at frequencies below 1 kHz at all SPLs is affected by increased low-frequency noise, typically caused by the ambient, primarily by mechanical vibrations in the dissection room.

Figure 6 shows the vibration-amplitude of different subjected cadaver skulls in dependence on the applied sound pressure, in the range of 40 to 90 dB SPL at 1000 Hz. The absolute value of the amplitude is calculated by the off-line signal processing, applied on two quasi-quadrature interferometric signals from photodiodes, acquired by the NI card. The total acoustic noise in the room was about 40 dB SPL, measured by B&K 2250 meter. The minimum amplitude, which we could accurately measure in these experiments was about 0.7 pm/ $\sqrt{\text{Hz}}$ . This value was determined by the environmental noise in the dissection room (fans in instruments, street noise, speech and mechanical vibration in the building) and the electronic noise of the measuring system (VCSEL intensity and frequency fluctuations, polarization noise, photodiode and transimpedance noise, ADC quantization noise). The largest vibration-amplitude of about 5 nm corresponds to the resonance peak at 90 dB SPL. In that way, a very high dynamic range of the system is confirmed – the amplitude span is over three orders of magnitude. Experimental results of head #05261 demonstrate a larger dissipation than others, which can be

explained by external noise associated with this measurement only. However, the linear trend, which has almost the same slope as in other experiments, is preserved. The minimum stable sound pressure used in this experiment of 40 dB SPL was limited by the Affinity audiometer's closed-loop characteristic and the environmental noise.

-----

Fig. 6

The vibration-amplitude of the incus has a linear response to the intensity of the acoustical excitation, with Pearson's  $r$  in all samples greater than 0.99. The sensitivities are quite different and are in the range of 0.25 to 5 nm/Pa @ 1 kHz. Such a span of sensitivity can primarily be attributed to the diversity of the anatomy and history of the cadaver skull, but also to the diversity of the points on the retroreflector onto the incus that are targeted by the laser beam. It is evident that is extremely important to hit the point of the highest amplitude of vibrations. This can be achieved by a careful adjustment and monitoring the output signals in real-time. Since the target point can be moved with the incus, it is important to have a reliable, uniform and good reflectivity across the entire retroreflector. We believe this issue could be solved in a final product by utilizing some other type of collimator and/or retroreflector. For example, we could employ a retroreflector made of glass beads of smaller diameter than currently used 30-50  $\mu\text{m}$ , uniformly distributed over the carrier substrate. Such a configuration will allow more effective light reflection, due to increased number of glass beads impinged at the same time by the optical beam emitted out of the collimator. Currently, the illuminated spot is determined by the mode-field diameter (MFD) at beam waist of the collimator of 62  $\mu\text{m}$ , which corresponds to one or maximum two or three illuminated glass beads in ideal case. Contrary, if the retroreflective glass beads have smaller diameter, for instance - of about 10  $\mu\text{m}$ , we will have between 25 and 30 beads taking place in the reflection of the beam at the same time. For further research, we plan to make a biocompatible retroreflector of titanium plate, covered with very small retroreflective glass beads. The glass beads will be bonded to the titanium plate by a medical-grade silicone resin, such as NuSil MED-6219, to assure a long-term fixation.

The amplitudes measured at a specific frequency are quite different, spanning over one decade, depending on the anatomy and history of the cadaver skull. Similar results concerning the frequency response and amplitude of ossicle vibrations of cadaver skulls are reported by other authors (Willi, 2003; Gan et al., 2010), which used the Polytec LDV device for measurement of the bone ossicles displacement. Some discrepancies between our and literature data exist, because we obtained about half the amplitude of vibrations at 90 dB SPL. However, it is

difficult to compare the results and explain this difference without knowledge of examined object history and experimental conditions. We believe that the main reason for this difference is the use of different ossicles as the target and diversity of aiming points over the ossicle. Our target was the short process of the incus, close to its head, which was not frequent in the previous work. Willi, 2003 and Whittemore et al., 2004 demonstrated a big influence of these factors on the displacement magnitude, due to the rather complex 3D distribution of modes of vibration of the bone ossicles, as reported by Dobrev et al., 2016 and Dobrev et al., 2018.

Figure 7 presents three pairs of frequency responses of the incus of the cadaver skull #05200, exposed to acoustical excitation of 50, 70, and 90 dB SPL. The spectrum pairs are calculated by the fast Fourier transform (FFT) applied on two sets of phase signals, outputted from the on- and off-line signal processing. The curves designated by HW are obtained from the analog output signals, produced in real-time by the DAC inside the TIFOS PCB, after the on-line signal processing. The off-line (SP) curves are obtained by calculation in MATLAB using the full ATAN algorithm (without approximation for ATAN function), applied on two raw photodiode signals, captured by NI DAQ, at the same time as the HW output signals. The points making the curves in Fig. 7 are the spectrum peaks at the acoustic excitation frequency, calculated by FFT bandwidth (BW) of 1 Hz.

Fig. 7

A very good match between the on-line captured and off-line calculated frequency responses exists for all sound pressure levels over the almost whole frequency range of interest. It confirms the proper operation of the algorithm, embedded into the Texas Instruments MSP432 microcontroller. Notice the absence of numerical values in the HW ordinate, because the voltage level of the DAC output can be arbitrarily set. In this case, the scale of about 100 mV/nm for the HW signal was adjusted until the two curves overlapped as much as possible, which was visually controlled on the graph. Such a setting was not the optimal scale in all cases - a dynamic changing of the scale value, which depends on the sound level in the space around the patient, can significantly improve the audibility at low and reduce the distortion at high SPLs. Similarly, the embedding of the  $\mu$ -law compression algorithm into the on-line processing software can further improve the system performance.

A difference between the signal amplitudes obtained by these two techniques can be noticed at low amplitudes and low frequencies of incus vibration (see wandering of the HW curve at 50 dB SPL in Fig. 7). When the vibration amplitude is very small, the signal obtained by the on-line processing has a lower SNR due

to higher quantization noise. Because of the ADC ADS8866 features (full span FS = 2.5V,  $2^{16}$  quantization levels) the worth of the least significant bit (LSB) is  $q = 38 \mu\text{V}$ , and the quantization noise is  $q/\sqrt{12} = 11 \mu\text{V}$ , in the on-line signal processing. Since the amplitude of the interferometric part of the photodiode signal was  $V_{A1} \approx 0.2 \text{ V}$ , and the laser wavelength  $\lambda = 1310 \text{ nm}$ , the sensitivity of the system was  $S \approx 2 \text{ mV/nm}$  (see the discussion below Equation (1)). Therefore, the quantization noise of  $11 \mu\text{V}$  corresponds to a vibration amplitude of about  $5.5 \text{ pm}$ , and, according to the curves in Fig. 7, the equivalent input acoustical noise (EIN) for sample #5200 was about  $50 \text{ dB SPL @ 1kHz}$ . Contrarily, in the off-line processing chain, where the NI DAQ performs A/D conversion, the output phase angle signal was not so affected by the quantization noise. Compared to the on-line processing, the quantization noise was  $8 \text{ dB}$  smaller (because the FS was set to  $0.4\text{V}$ ), and the EIN in the case of sample #5200 was about  $42 \text{ dB SPL}$ . Notice that there is no single value of EIN associated with the optoelectronic system itself - although many system elements significantly affect its value, the EIN is mostly determined by the response of the examined head to an acoustic stimulus.

A discrepancy between two signal processing is especially evident at low frequencies, between  $100 \text{ Hz}$  and  $500 \text{ Hz}$ . This is because the quantization noise has a non-uniform distribution when the sinusoidal voltage to be digitized has a very small amplitude, in the range of quantization noise. In such a case, the spectral distribution depends strongly on the sampling rate/signal frequency ratio and the signal/noise amplitude ratio and is higher at lower frequencies (Widrow and Kollár, 2008). Also, the low-pass filters applied on the output signal significantly reduce both the signal and the noise at frequencies above  $4\text{-}5 \text{ kHz}$ , also reducing the difference between HW and SP signals at higher frequencies.

A way to improve SNR is to reduce the quantization noise by increasing the ADC resolution. Unfortunately, ADCs with higher resolutions have either unacceptable higher power consumption or insufficient conversion speed. However, the value of LSB in a 16-bit ADC can effectively be decreased by properly adjusting the input span - FS. Improvement can be obtained by dynamically setting the upper and lower limits of digitization based on monitoring of the actual photodiode signal range, using an ADC that has this functionality (ADS8866 is not one of these).

The effect of frequency up-conversion always exists in an interferometric system, following even slight changes in the phase angle and the frequency spectra of the photodiode signals depend linearly on the incus velocity (Durst et al., 1976). Using the suitable signal processing described above, we virtually maintained the operating point of the interferometer at maximum sensitivity, ensuring that the output phase signal is

proportional to the displacement in a large dynamic range. However, to properly process a large incus displacement, two conditions had to be satisfied: a) the displacement must not be too fast for our ADC sampling rate, and b) the displacement must not be too large for our DAC dynamic range.

If the incus movement is too fast, in the way that the highest frequency in the photodiode signal is higher than half of the ADC sampling rate (16 kHz), the signal will not be properly digitized. For this reason, some impacts, larger movements and stronger vibrations even in the frequency range less than 100 Hz will not be demodulated correctly by the microcontroller. They will be transposed into the acoustical frequency domain, where they will be overlapped with the audio signal of interest. Because of that, it is impossible to filter them out of the final signal. In audio recordings, obtained either in the on-line or the off-line signal processing, this additional noise can be heard as squeaks, whistles, or humming noises, which do not exist in the real environment. Such errors occur occasionally and can be noticed, for example, in supplements - in Martin Luther King's speech at the 82<sup>nd</sup> second and Theresa May's speech at the 62<sup>nd</sup> second. Increasing the sampling rate of ADC will help the algorithm to avoid such up-conversions and recover the full incus path.

If the displacement is too large, a properly recovered phase angle signal which follows the incus path can hit the DAC boundaries in the on-line processing chain. If we want to generate an analog signal where the smallest step corresponds roughly to 10 pm, the equivalent displacement the DAC maximal voltage output is only about 650 nm, because a 16-bit DAC has 65536 discrete levels. If a slow movement is larger than that, a clipping occurs. In audio recordings, such a DAC clipping usually sounds like distortion or crackle. This can be heard in the audio supplementary material Netrebko\_La-Traviata\_52-80dBA.mp3, at the 10<sup>th</sup>, 16<sup>th</sup>, 22<sup>nd</sup>, 27<sup>th</sup> and 81<sup>st</sup> second. In these events, it can be noticed that the clipping is not related to the actual amplitude of the audio signal. The noise spectrum cannot be accurately measured in such a case, because it strongly depends on the rate of occurrence and duration of clipping.

Notice that DAC clipping does not appear in the off-line signal processing: MATLAB uses float-point numbers, and the output phase angle can be arbitrarily large. This is another cause of the difference between the signals obtained by the two processing techniques. In the on-line processing, the problem could easily be solved using a DAC with more bits, or by applying the digital audio bandpass filter within the processing algorithm, before sending the calculated phase angle to the DAC. However, we did not have enough processing time in the interval between the two consecutive samples to apply this, relatively simple operation.



We could not apply any of the possibilities mentioned here (digital filtering,  $\mu$  - law, higher sampling rate, adjustable input span) to improve the SNR of the HW signal, because that would require an increase in the master clock of the microcontroller. A higher clock increases the electrical current consumption, which then would become higher than 10 mA, set as the target value for the whole TIFOS device. In the future, however, it will certainly be possible using a new generation of low-power microcontrollers, improved operational amplifiers and VCSELs. Also, we expect that we will develop a more efficient algorithm for the on-line signal processing, which will not work at the level of one sample, but on a block of many photodiode signal values, which number will be limited by the maximum allowed signal delay.

In the supplements, a few audio recordings in a time duration of about 1-3 min, which are acquired during experiments performed on the cadaver skull #7587, are provided. The signals have been on-line processed by the TIFOS system and recorded by an HP notebook audio-card without any frequency equalizing. The sound pressure level was measured by B&K 2250 sound meter (dBA, slow). The sound of the piano and violin in Schuberts Rondo in Fig. S1a is of a high fidelity. High-frequency tones in the aria from “La-Traviata” performed by Anna Netrebko are also very clear and dynamic. The famous speech of Martin Luther King is completely intelligible, as well as the resignation speech of Theresa May. The individual characteristics of well-known voices are easily recognizable.

Fig. S2 demonstrates REUR signals of subjected heads presented in Fig. 5 and Fig. 6. Generally, the REUR signals are similar revealing the resonance frequency in the range of 2000 Hz to 4000 Hz caused by natural amplification by the outer ear and ear canal, but there are specific individual differences in the frequencies of maximal peaks.

#### 4. Conclusion

We developed a model of a sensing system capable of measuring the acoustic incus vibrations in the middle ear of a human being. The system was experimentally tested on cadaver skulls. The interferometric fading is solved using the two quasi-quadrature signals produced by the 3x3 single-mode fiber optic coupler, and the special signal processing algorithm, based on the inverse tangent function. The optoelectronic module, made in a size suitable for implantation, performs the signal processing in real-time and generates an audio signal of such a quality, which allows the overall system to be used as an implantable microphone. The optomechanical holder enables long-term stability by fixing the sensing probe onto the skull bone and directing the laser beam towards

the incus. The minimum experimentally measured amplitude at low sound pressure of 40 dB SPL was in the picometer domain, while the maximum, at 90 dB SPL, was about a few nanometers. A wide dynamic span over the whole acoustic frequency range, including high-frequency tones, leading to natural and clear sounds and excellent dynamics was also demonstrated by the on-line recording of some sequences of music, speech, and interviews. We expect that the amplitude of the incus vibration in living human beings will be larger, which may further improve the sound quality. In future work, we intend to integrate the TIFOS microphone with a cochlear implant to make a totally implantable device.

mmc1.mp3

mmc2.mp3

mmc3.mp3

mmc4.mp3

mmc5.docx

Declaration of interests

None.

## Acknowledgements

The authors thank the Niederösterreichische Forschungs- & Bildungsgesellschaft (NFB) for sponsoring this work by Life Science grant: LS14-026 and ACMIT GmbH for the support of the project. M. T. thanks to Ministry of Education, Science and Technological Development of Serbia to support him in this investigation, in the frame of the agreement 451-03-68/2020-14/200175 with ITS-SASA. We further thank Julia Dworan and the deceased Istvan Paraszti for their help in preparing the cadaver heads and material in the Center of Anatomy. Finally, we thank Nina Tomic for preparing the figures.

## 1    **References**

- 2    Briggs, R. J. S., Eder, H. C., Seligman, P. M., Cowan, R. S. C., Plant, K. L., Dalton, J., Money, D. K. Patrick, J.  
3    F., 2008, Initial clinical experience with a totally implantable cochlear implant research device, *Otol. Neurotol.*  
4    29, 114-119.
- 5    Bittencourt, A.G., Burke, P.R., de Souza Jardim, I., de Brito, R., Tsuji, R.K., de Oliveira Fonseca, A.C., Bento,  
6    R.C., 2014. Implantable and semi-implantable hearing aids: a review of history, indications, and surgery. *Int*  
7    *Arch Otorhinolaryngol.* 18, 303–310.
- 8    Bruchhage, K.L., Leihle, A., Shönweiler, R., Todt, I., Baumgartner, W.D., Frenzel, H., Wollenberg, B., 2017.  
9    Systematic review to evaluate the safety, efficacy and economical outcomes of the Vibrant Soundbridge for the  
10    treatment of sensorineural hearing loss. *Eur Arch Otorhinolaryngol* 274,1797–1806
- 11    Bruschini, L. Berrettini, S., Forli, F., Murri, A., Cuda, D., 2016. The Carina© middle ear implant: surgical and  
12    functional outcomes. *Eur Arch Otorhinolaryngol* 273, 3631-3640.
- 13    Bruschini, L., Forli, F., Santoro, A., Bruschini, P., Berrettini, S. 2009. Fully implantable Otologics MET Carina  
14    device for the treatment of sensorineural hearing loss. Preliminary surgical and clinical results. *Acta*  
15    *Otolaryngol.* 29, 79–85.
- 16    Calero, D., Paul, S., Gesing, A., Alves, F., Cordioli, J.A., 2018. A technical review and evaluation of  
17    implantable sensors for hearing devices. *BioMed Eng OnLine* 17, 23.
- 18    Calero, D., Paul, S., Cordioli, J.A., 2016. On implantable sensors for totally implantable hearing aids. In:  
19    *Proceedings: 5th Joint Meeting of the ASA and ASJ, Honolulu, Hawaii.*
- 20    Chen, D.A., Backous, D.D., Arriaga, M.A., Garvin, R., Kobylek, D., Littman, T., Walgern, S., Lura, D., 2004.  
21    Phase 1 clinical trial results of the Envoy System: a totally implantable middle ear device for sensorineural  
22    hearing loss. *Otolaryngol Head Neck Surg* 131, 904-916.
- 23    Dettman, S.J., Dowell, R.C., Choo, D., Arnott, W., Abrahams, Y., Davis, A., Dornan, D., Leigh, J.,  
24    Constantinescu, G., Cowan, R., Briggs, R.J., 2016. Long-term communication outcomes for children receiving  
25    cochlear implants younger than 12 months: a multicenter study. *Otol Neurotol.* 37, 82–95.

- 1 Didyk, L.A., Bogdanov, V.B., Lysenko, V.A., Didyk, N.P., Gorgo, Y.P., Dirckx, J.J., 2006. The effects of slight  
2 pressure oscillations in the far infrasound frequency range on the pars flaccida in gerbil and rabbit ears. *Int. J.*  
3 *Biometeorol.* 51, 221–231.
- 4 Dirckx, J.J.J., Buytaert, J.A.N, Decraemer, W.F., 2006. Quasi-static transfer function of the rabbit middle ear,  
5 measured with a heterodyne interferometer with high-resolution position decoder. *JARO* 7, 339-351.
- 6 Djinović, Z., Pavelka, R., Tomić, M., Sprinzl, G., Plenk, H., Losert, U., Bergmeister, H., Roberto Plasenzotti,  
7 R., 2018. In-vitro and in-vivo measurement of the animal's middle ear acoustical response by partially  
8 implantable fiber-optic sensing system. *Biosens Bioelectron* 103, 176-181.
- 9 Dobrev, I., Ihrle, S. Rösli, C., Gerig, R., Eiber, A., Huber, A.M., Sim, J.H., 2016. A method to measure sound  
10 transmission via the malleus-incus complex. *Hear. Res.* 340, 89-98
- 11 Dobrev, I., Sim, J.H., 2018. Magnitude and phase of three-dimensional (3D) velocity vector: Application to  
12 measurement of cochlear promontory motion during bone conduction sound transmission. *Hear. Res.* 364, 96-  
13 103
- 14 Durst, F., A. Melling, A., Whitelaw, J.H., 1976. Principles and practice of laser-Doppler anemometry,  
15 Academic Press, New York.
- 16 Eggermont, J.J., 2017. Hearing loss, Academic Press, Calgary.
- 17 Faes, J., Gillis, S., 2019. Auditory brainstem implantation in children with hearing loss: Effect on speech  
18 production. *Int. J. Pediatr. Otorhinolaryngol.* 119, 103–112.
- 19 Gao, N., Chen, Y.Z., Chi, F.L., Zhang, T.Y., Xu, H.D., Kang, H. Y., Pan, T.Z., 2013. The frequency response  
20 of a floating piezoelectric microphone for the implantable middle ear microphone. *Laryngoscope*, 123, 1506–  
21 1513.
- 22 Gan, R.Z., Dai, C., Wang, X. Nakmali, D., Wood, M.W., 2010. A totally implantable hearing system – design  
23 and function characterization in 3D computational model and temporal bones. *Hear. Res.* 263, 38–144.
- 24 Gerard, J.M., Domanez, L., Salmon, C., Vanpoucke, F., Walraevens, J., Plasmans, A., De Siati, D., Lefebvre,  
25 P., 2017. Feasibility of an implanted microphone for cochlear implant listening. *Eur Arch Otorhinolaryngol*  
26 274, 1383–1390.

- 1 Gesing, A.L., F. Alves, F.D.P., Paul, S., Cordioli, J.A., 2018. On the design of a MEMS piezoelectric  
2 accelerometer coupled to the middle ear as an implantable sensor for hearing devices. *Sci. Rep.* 8, 3920-3930.
- 3 Grossöhmichen, M., Salcher, R., Kreipe, H.H., Lenarz, T., Maier, H., 2015. The Codacs™ direct acoustic  
4 cochlear implant actuator: exploring alternative stimulation sites and their stimulation efficiency. *PLoS ONE*  
5 10, e0119601.
- 6 Hammer, M.S., Swinburn, T.K., Richard, L.N., 2014. Environmental noise pollution in the United States:  
7 developing an effective public health response. *Environ. Health Perspect.* 122, 115–119.
- 8 Haynes, D.S., Young, J.A., Wanna, G.B., Glasscock, M.E., 2009. Middle ear implantable hearing devices: an  
9 overview. *Trends Ampli.* 13, 206-214.
- 10 Hüttenbrink, K.B., 1988. The mechanics of the middle-ear at static air pressures: the role of the ossicular joints,  
11 the function of the middle-ear muscles and the behaviour of stapedial prostheses. *Acta Otolaryngol Suppl.* 451,  
12 1-35.
- 13 Ihrle, S., Gerig, R., Dobrev, I., Roeoesli, C., Sim, J.H., Hubber, A.M., Eiber, A., 2016. Biomechanics of the  
14 incudo-malleolar-joint - experimental investigations for quasi-static loads. *Hear. Res.* 340, 69-78.
- 15 Jenkins, H.A., Atkins, J.S., Horlbeck D., Hoffer M.E., Balough B., Arigo, J.V., Alexiades, G., Gavris, W.,  
16 2007. US Phase I preliminary results of use of the Otologics MET fully-implantable ossicular stimulator.  
17 *Otolaryngol Head Neck Surg* 137, 206–212.
- 18 Jenkins, H.A., Atkins, J.S., Horlbeck, D., Hoffer, M.E., Balough, B., Alexiades, G., Garvis, W., 2008. Otologics  
19 fully implantable hearing system: phase I trial 1-year results. *Otol Neurotol.* 29, 534-541.
- 20 Jia, X.H., Gao, N., Xu, X.X., Wu, Y.Z., Kang, H.Y., Chi, L.F., 2016. A new floating piezoelectric microphone  
21 for the implantable middle ear microphone in experimental studies. *Acta Oto-Laryngologica* 136, 1248-1254.
- 22 Klein, K, Nardelli, A., Stafinski, T., 2012. A Systematic Review of the Safety and Effectiveness of Fully  
23 Implantable Middle Ear Hearing Devices: The Carina and Esteem Systems. *Otology & Neurotology* 33, 916-  
24 921
- 25 Klein, K, Nardelli, A., Stafinski, T., 2013. A Systematic Review of the Safety and Effectiveness of the Vibrant  
26 Soundbridge. *J Otol Rhinol* 2:3

- 1 Ko, W.H., Zhang, R., Huang, P., Guo, J., Ye, X., Young, D.J., Megerian, C.A., 2009. Studies of MEMS  
2 acoustic sensors as implantable microphones for totally implantable hearing-aid systems. *IEEE Trans Biomed*  
3 *Circuits Syst.* 3, 277–85.
- 4 Koch, M., Essinger, T.M., Bornitz, M., Zahnert, T., 2014. Examination of mechanical amplifier in the  
5 incudostapedial joint gap: FEM simulation and physical model. *Sensors* 14, 14356–14374.
- 6 Komori, M., Yanagihara, N., Hinohira, Y., Hato, N., Gyo, K., 2010. Long-term results with the Rion E-type  
7 semi-implantable hearing aid. *Otolaryngology–Head and Neck Surgery* 143, 422–428
- 8 Koo, K.P., Tveten, A.B., Dandridge, A., 1982. Passive stabilization scheme for fiber interferometers using (3×  
9 3) fiber directional couplers. *Appl. Phys. Lett.* 41, 616–618.
- 10 Kozlowski, K., Friedland, D.R., 2014. Implantable hearing devices. *Curr Surg Rep* 2, 59.
- 11 Lenarz T., 2017. Cochlear implant – state of the art. *GMS Curr Top Otorhinolaryngol Head Neck Surg.* 16,  
12 Doc04.
- 13 Leysieffer, H., Baumann, J.W., Mayer, R., Müller, D., Müller, G., Schön, T., Volz, A., Zenner, H.P., 2003. A  
14 totally implantable hearing aid for inner ear deafness: TICA LZ 3001. *HNO* 46, 853–863.
- 15 Lieu, J.E.C., 2004. Speech-language and educational consequences of unilateral hearing loss in children. *Arch.*  
16 *Otolaryngol. Head. Neck Surg.* 130, 524–530.
- 17 Lyons, R.G., 2012. Streamlining digital signal processing: a trick of the trade guidebook, Wiley-IEEE Press,  
18 New Jersey.
- 19 Maniglia, A.J., Murray, G., Arnold, J.E., Ko, W.H., 2001. Bioelectronic microphone options for a totally  
20 implantable hearing device for partial and total hearing loss. *Otolaryngol Clin N Am.* 34, 469–483.
- 21 Memari, F., Asghari, A., Daneshi, A., Jalali, A., 2011. Safety and patient selection of totally implantable  
22 hearing aid surgery : Envoy system, Esteem. *Eur Arch Otorhinolaryngol* 268, 1421–1425.
- 23 Murali, S., Krishnan, P.V., Bansal, T., Karthikeyan, K., Natarajan, K., Kameswaran, M., 2009. Totally  
24 implantable hearing aid surgical technique and the first Indian experience with Envoy esteem. *Indian J*  
25 *Otolaryngol Head Neck Surg* 61, 245–251.

- 1 Park, S., Guan, X., Kim, Y., Creighton, F.P.X., Wei, E., Kymissis, I.J., Nakajima, H.H., Olson, E.S., 2018.
- 2 PVDF-based piezoelectric microphone for sound detection inside the cochlea: toward totally implantable
- 3 cochlear implants. *Trends Amplif.* 22, 1–11.
- 4 Park, W.T., O'Connor, K.N., Chen, K.L., Mallon Jr. J.R., Maetani, T., Dalal, P., Candler, R.N., Ayanoor-
- 5 Vitikkate, V., Roberson Jr., J.B., Puria, S., Kenny, T.W., 2007. Ultraminiature encapsulated accelerometers as a
- 6 fully implantable sensor for implantable hearing aids. *Biomed. Microdevices* 9, 939–949.
- 7 Pavelka, R., Vujanic, A., Djinojic, Z., Mitic, S., Vujanic, D., Kment, Ch., Tomic, M., 2003. Animal
- 8 Experiments with a fiber-optic vibrometer to be used as a microphone for totally implantable cochlear and
- 9 middle ear implants. In: *Proceedings: 4th International symposium on electronic implants in otology &*
- 10 *conventional hearing aids*, Toulouse, France.
- 11 Pulcherio, J.O., Bittencourt, A.G., Burke, P.R., da Costa Monsanto, R., de Brito, R., Tsuji, R.K., Bento, R.F.,
- 12 2014. Carina® and Esteem®: a systematic review of fully implantable hearing devices. *PLoS One* 9, e110636.
- 13 Seong, K.W., Mun, H.J., Shin, H.D., Kim, J.H., Nakajima, H.H., Puria, S., Cho, J. H., 2019. A vibro-acoustic
- 14 hybrid implantable microphone for middle ear hearing aids and cochlear implants. *Sensors* 19, 1117-1131.
- 15 Shohet, J.A., Gende, D.M., Tanita, C.S., 2018. Totally Implantable Active Middle Ear Implant: Hearing and
- 16 Safety Results in a Large Series. *Laryngoscope*, 128, 2872–2878.
- 17 Silverstein H., Atkins J., Thompson J. H., Jr., Gilman N., 2005. Experience with the SOUNDTEC implantable
- 18 hearing aid. *Otology & Neurotology*, 26, 211-217.
- 19 Tay, H.L., Mills, R.P., 1996. The mobility of the malleus and incus with varying middle ear pressures. *Clin.*
- 20 *Otolaryngol.* 21, 256-258.
- 21 Tisch, M., 2017. Implantable hearing devices. *GMS Curr Top Otorhinolaryngol Head Neck Surg.* 16, Doc06.
- 22 Tomic, M.C., Djinojic, Z.V., Petricevic, S.J., 2017. Demodulation of quasi-quadrature interferometric signals
- 23 use in the totally implantable hearing aids. *Biomed. Opt. Express* 8, 3404–3409.
- 24 Vujanic, A., Pavelka, R., Adamovic, N., Kment, C., Mitic, S., Brenner, W., Popovic, G., 2002. Development of
- 25 a totally implantable hearing aid. In: *Proceedings: 23rd international conference on microelectronics, MIEL,*
- 26 *Nis, Yugoslavia.*

- 1 Widrow B. and Kollár I. (2008), Quantization Noise - Roundoff Error in Digital Computation, Signal
- 2 Processing, Control, and Communications, Cambridge University Press, New York, USA
- 3 Whittemore Jr., K.R., Merchant, S.N., Poon, B.B., Rosowski, J.J., 2004. A normative study of tympanic
- 4 membrane motion in humans using a laser Doppler vibrometer (LDV). *Hear. Res.* 187, 85–104.
- 5 Willi, U.B., 2003. Middle-ear mechanics: the dynamic behavior of the incudo-malleolar joint and its role during
- 6 the transmission of sound (Ph.D. Thesis). Uni. Zürich, Zürich.
- 7 Woo, S.H.A., Woo, S.T., Song, B.S., Cho, J.H., 2013. Feedback characteristics between implantable
- 8 microphone and transducer in middle ear cavity. *Biomed Microdevices* 15, 867–877.
- 9 Woo, S.T., Shin, D.H., Lim, H.G., Seong, K.W., Gottlie, P., Puria, S., Lee, K.Y., Cho, J.H., 2015. A new trans-
- 10 tympanic microphone approach for fully implantable hearing devices. *Sensors* 15, 22798-22810.
- 11 Wray, C.M., Thaler, E.R., 2016. Hypoglossal nerve stimulation for obstructive sleep apnea: a review of the
- 12 literature. *WJOHNS* 2, 230-233.
- 13 Young, D., P. Cong, P., 2019. Wireless implantable sensors: from lab to technology breakthrough ambitions.
- 14 *Sens. Actuator. A Phys.* 294, 81–90.
- 15 Zargarpour, N., Zarifi, M.H., 2015. A piezoelectric micro-electromechanical microphone for implantable
- 16 hearing aid applications. *Microsyst. Technol.* 21, 893–902.
- 17 Zenner, H.P., Leysieffer, H., 2001. Total implantation of the imply TICA hearing amplifier implant for high-
- 18 frequency sensorineural hearing loss: the tübingen university experience. *Otolaryngol. Clin. North Am.* 34,
- 19 417–446.
- 20 Zernotti, E.M., Sarasty, A.B., 2015. Active bone conduction prosthesis: Bonebridge<sup>TM</sup>. *Int Arch*
- 21 *Otorhinolaryngol* 19, 343–348.
- 22 Zhang, B.Y., Young, Y.H., 2019. Declining prevalence of pediatric sudden deafness during the past two
- 23 decades. *Int. J. Pediatr. Otorhinolaryngol.* 119, 118–122.
- 24 Zwartenkot, J.W., 2017. Auditory implants in otology-active middle ear implants and direct acoustic cochlear
- 25 stimulation: indications and outcome (Ph.D. Thesis). Radboud University, Nijmegen.



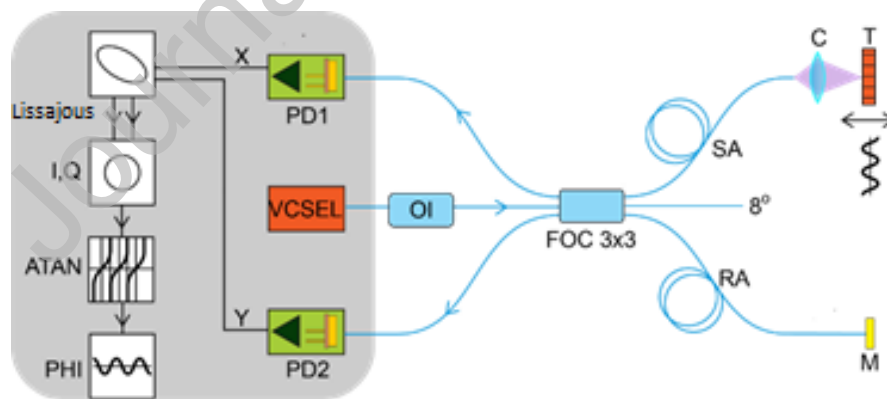


Fig. 1

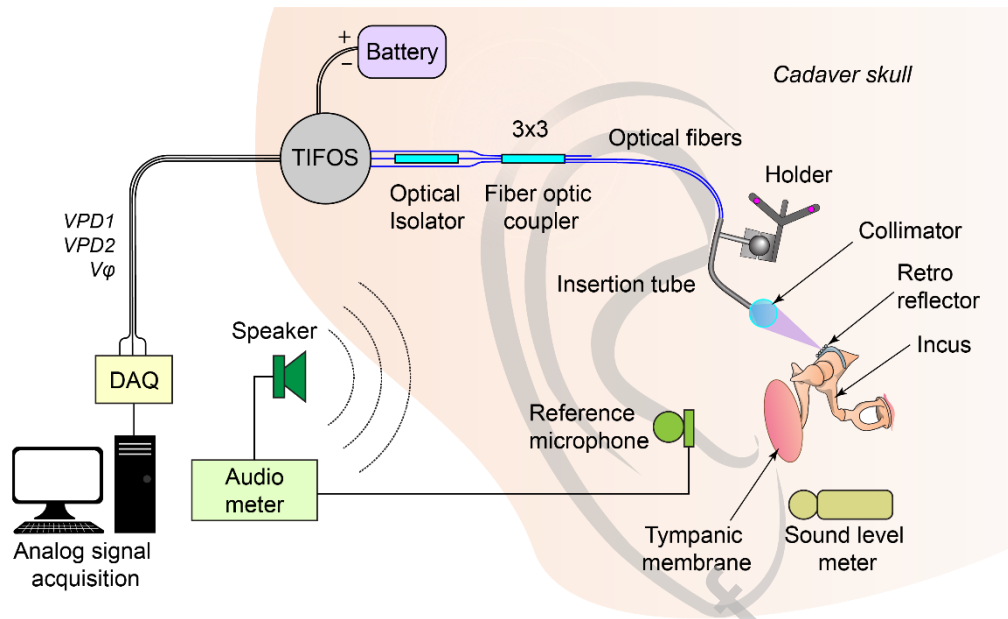


Fig. 2

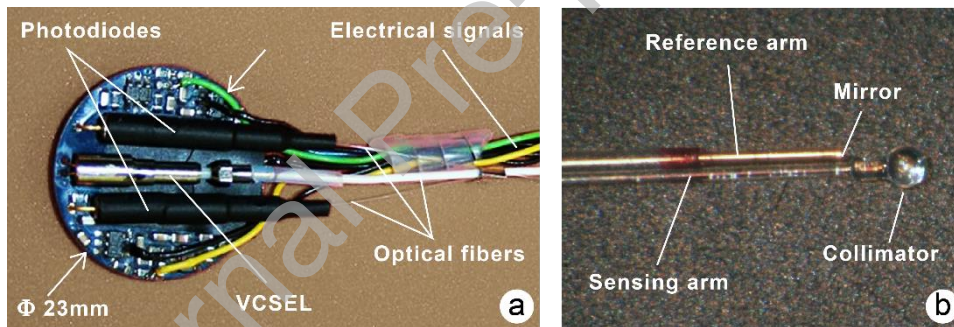


Fig. 3

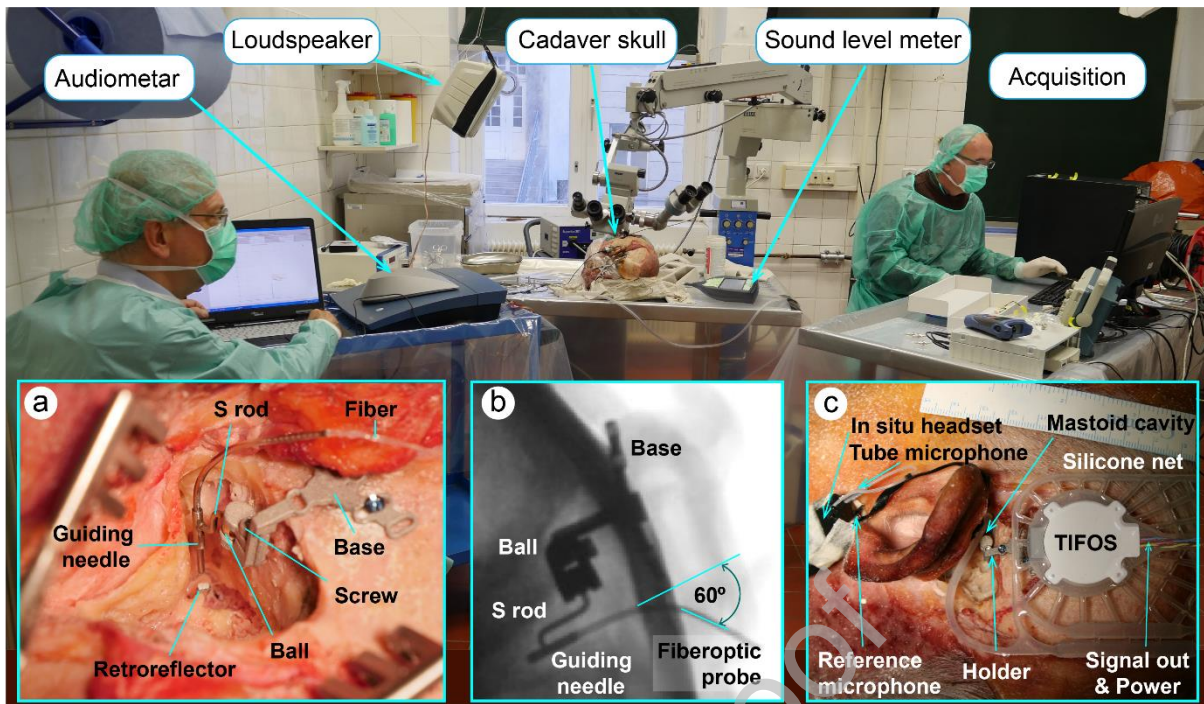


Fig. 4

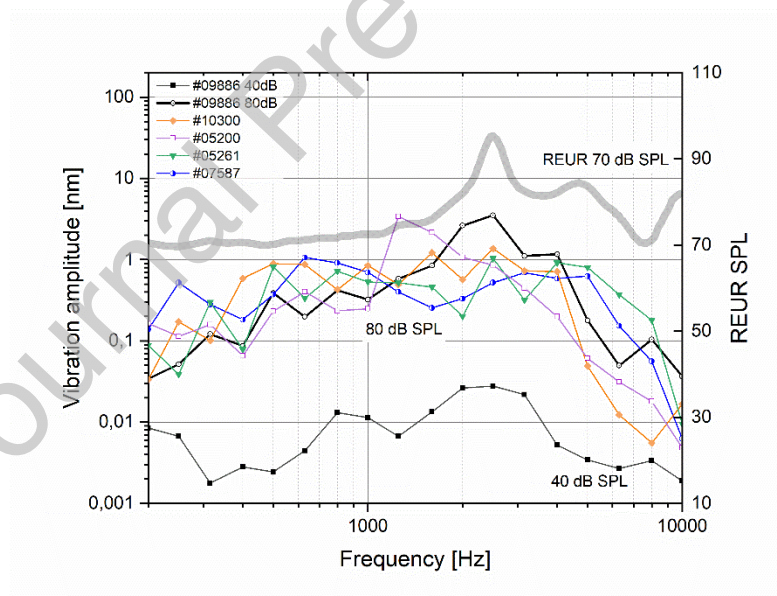


Fig. 5

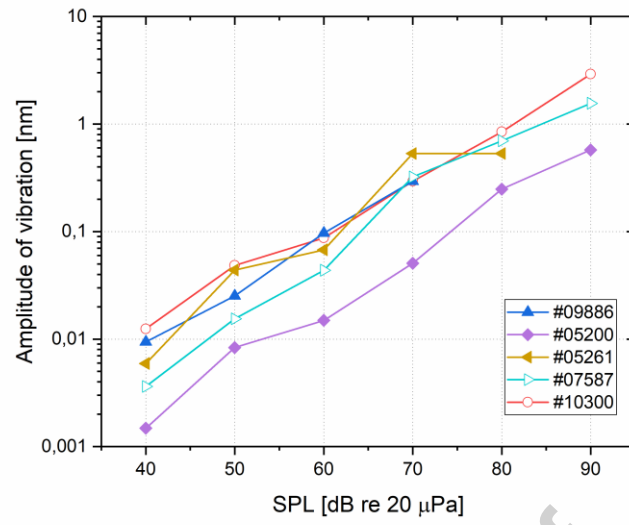


Fig. 6

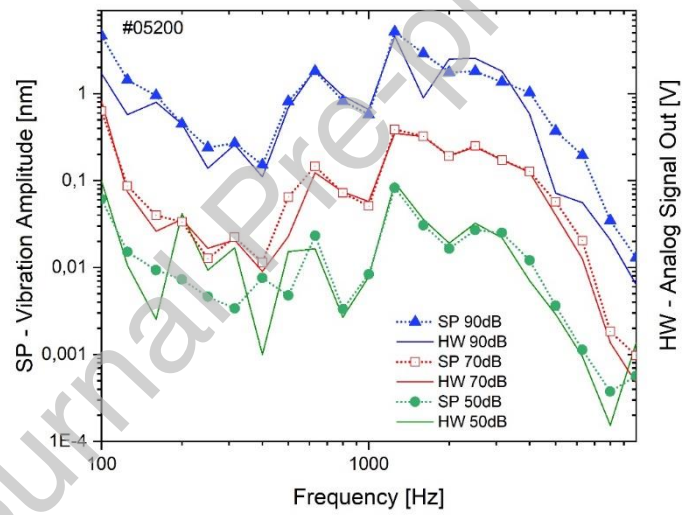


Fig. 7

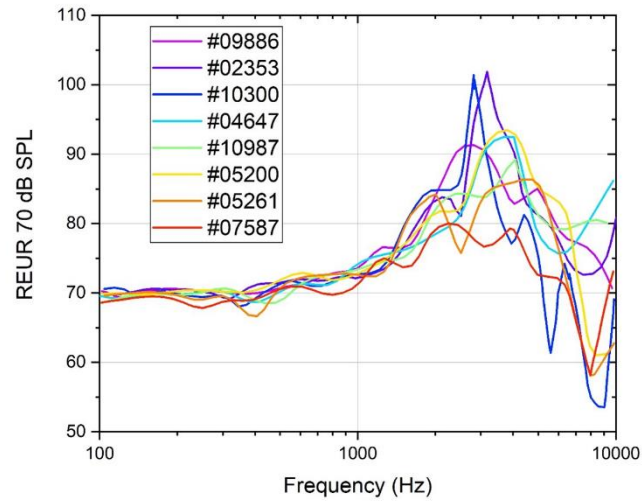


Fig. S2